LBNL-1002E

CBP-795

Electron Cloud Cyclotron Resonances in the Presence of a Short-bunch-length Relativistic Beam *

C. M. Celata[a], Miguel A. Furman, J.-L. Vay, and Jennifer W. Yu[b]

Lawrence Berkeley National Laboratory

1 Cyclotron Road, Berkeley, CA 94720, U.S.A.

Abstract

Computer simulations using the 2D code "POSINST" were used to study the formation of the electron cloud in the wiggler section of the positron damping ring of the International Linear Collider. In order to simulate an x-y slice of the wiggler (i.e., a slice perpendicular to the beam velocity), each simulation assumed a constant vertical magnetic field. At values of the magnetic field where the cyclotron frequency was an integral multiple of the bunch frequency, and where the field strength was less than approximately 0.6 T, equilibrium average electron densities were up to three times the density found at other neighboring field values. Effects of this resonance between the bunch and cyclotron frequency are expected to be non-negligible when the beam bunch

---

* This work was supported by the Office of Science, U. S. Department of Energy, under Contract No. DE-AC02-05CH11231.

[a] Visitor; California Institute of Technology; Physics, Mathematics, and Astronomy, CMCelata@lbl.gov

[b] Presently a student at Cornell University, Ithaca, NY, U.S.A.

length is much less than the product of the electron cyclotron period and the beam velocity, for a beam moving at v≈c. Details of the dynamics of the resonance are described.

PACS: 29.27Bd, 29.20db

I. Introduction

In circular accelerators or storage rings with beams at high energy, electrons can be produced by the interaction of beam synchrotron radiation with the vacuum wall, by lost beam particles striking the wall, or by ionization of background gas. These "primary electrons" then produce secondary electrons upon impact with the vacuum wall. This process can lead to an "electron cloud" of sufficient density to negatively impact beam stability and quality [1]. Electron cloud effects are particularly strong for beams of positive particles, since negative beams repel electrons, keeping them near the wall where they tend to interact more weakly with the beam and also are lost more quickly. Due to the quest for the highest possible collider beam luminosity, which then requires high bunch intensity and frequency, electron cloud effects are an important issue in all state-of-the-art accelerators for high-energy physics, as well as in high-intensity accelerators for nuclear physics and heavy-ion-driven inertial fusion [1,2]. In the International Linear Collider (ILC) design, electron cloud effects are expected to be important in the positron damping rings, where bending of the beam in dipoles and wigglers produces copious synchrotron radiation, and hence a large number of photoelectrons.

In order to investigate this issue, a series of computer simulations was performed for the parameters of the wigglers of the ILC positron damping ring using the two-dimensional computer code POSINST [3-5]. In each simulation the field of an ideal dipole was imposed (i.e., a static uniform magnetic field in the vertical (+y) direction, where the beam is assumed to be traveling in the +z direction). Each simulation thus was a simplified representation of an x-y slice of the wiggler. The calculations (which simulate an interval of 500 bunch passages) covered the "buildup" phase-- i.e., the electron cloud formation-- which takes place over a time interval of a few microseconds (~200 bunch passages) for present ILC parameters. In this time the density of the electrons in the vacuum chamber first increases, then plateaus at what will be referred to here as its "equilibrium" value, since this value represents an equilibrium between electron production and loss. POSINST assumes the distribution function of the beam to be unaffected by the electron cloud, which is a reasonable assumption for this timescale. The cloud evolution was calculated for the range of magnetic field values expected in the wiggler, i.e., B = 0 – 1.6 T.

Results of the simulations showed very little dependence of the equilibrium cloud average density (i.e., the electron density at the density plateau averaged over the vacuum chamber volume) on B for B greater than approximately 0.6 T. But below this value there were magnetic field values for which the average cloud density was enhanced by factors of up to 3 over the density at nearby magnetic field values. The magnetic fields at which this enhancement occurred have been identified as fields at which the bunch

spacing (i.e., the time between the arrival of one beam bunch and the next) is an integral multiple of the electron cyclotron frequency. At these fields the resonance condition

$$B = n\frac{2\pi m_e}{e\tau_b} \tag{1}$$

is fulfilled, where τ_b is the bunch spacing, m_e is the electron rest mass, $-e$ is the electron charge, with n equal to a positive integer. This is a plausible situation for resonant behavior, since each time a beam bunch appears electrons will be at the same position in their cyclotron orbit if relativistic mass increase can be neglected. Electrons are born at the walls at very low energy and this nonrelativistic approximation is therefore true for some part of their lifetime in the system. As will be shown below, almost all electrons leave the system before any appreciable mass increase occurs. It is also to be noted that all of the electrons in the system for which the relativistic mass increase is negligible are in resonance, since the magnetic field is constant throughout the cross section. Thus the resonance can have a significant effect on the whole cloud.

There are two somewhat similar resonances to those we have found that have been mentioned in the literature. Rumolo and Zimmerman in reference [6] showed a very similar phenomenon that was a resonance between ion cyclotron motion and the bunch passage. Because of the large ion gyroradius and two-species nature of the problem, the dynamics in their case were in detail somewhat different from what is discussed here, but the resonance is similar. In the other instance, Cai et. al. in reference [7] discussed an increase in the electron cloud density for a case where the vacuum chamber was surrounded by a solenoid. The increase occurred when the bunch period was equal to

half the electron cyclotron period. The dynamics they discuss, however, were quite different from the dynamics described in this paper. The resonance with which they were dealing was the multipacting resonance. Because of the solenoidal field, the distance the electron traveled from birth to the time it hit the wall again was not the width of the vacuum chamber as in the usual case, but rather the length of a cyclotron orbit. Therefore the cyclotron period appeared in the multipacting resonance condition. In contrast, in the ILC wiggler case we examine here, the electron stays in resonance with the bunch through several bunch passages and the increase in the cloud density is due to an increase in electron perpendicular energy due to synchronization of the bunch appearance with the cyclotron orbit.

In this report we will discuss the cause of the high electron cloud density at the magnetic fields at which the resonance condition is fulfilled. We will also describe the dynamics of the electron cloud formation there, and propose a reason that such an effect is not seen at higher field or for long bunches. In Section II the computational model and parameters for the simulations are described. Section III describes the simulation results. In Section IV the results of a tracking code for individual particle dynamics are used to elucidate the dynamics of the resonance process. Section V compares the simulation and single particle results and contains further discussion of the dynamics of electrons in resonance. In Section VI special features at high and low magnetic field are explained. Results of an analytical model are given in Section VII. Both the analytical model and the single particle tracking have simplifying assumptions and do not reflect the full dynamics calculated in POSINST. But they add considerable insight, and each complements the

other, since the single-particle tracking reflects the situation well at low B and has no constraint on electron phase space, whereas the analytical model is good for all B and thus can explain important features at high B, but is restrictive in the phase space treated. Conclusions are discussed in Section VIII.

II. The Computational Model and Parameters

The model used by POSINST is described in several publications [3-5]. The system we have simulated is an x-y slice of the accelerator in the plane perpendicular to the direction of beam propagation (+z). A constant uniform magnetic field is applied in the vertical (+y) direction. Table I gives numerical and physical parameters used for all the simulations described in this report.

The beam bunch density is assumed to be Gaussian in x, y, and z, with the bunch centroid centered transversely in the vacuum chamber. The beam distribution function does not evolve with time in these calculations. We assume that this is a reasonable approximation for the few microseconds required for the electron cloud buildup. The bunch centroid passes through the center of the vacuum chamber—no attempt is made here to include the details of the centroid orbit in the wiggler.

The beam magnetic field is neglected in POSINST since its force is negligible compared to the beam electric field because the electrons are at low velocity. As can be seen

below, even though the energy of electrons increases due to the resonance, essentially all have energies small enough that the nonrelativistic approximation remains valid. POSINST uses a particle-in-cell (PIC) algorithm to calculate the time-evolving electric field of the electrons and to apply this field to their motion.

Table 1. Parameters used for all simulations described in this report.

Quantity	Value
Positrons per beam bunch, N_b	2.0×10^{10}
Positron energy	5 GeV
Bunch spacing, τ_b	6.15 ns
σ_x (beam)	112 μm
σ_y (beam)	4.6 μm
σ_z (beam)	6.0 mm
Full bunch length	$\pm 2.5\ \sigma_z$
Photons emitted per positron per meter	0.07
Quantum efficiency	0.1
Peak secondary electron yield at normal incidence	1.4
PIC spatial grid cell size	0.36 mm
Integration Time Step	1.25×10^{-11} s
Vacuum pipe radius, a	2.3 cm

The photons emitted by the beam are assumed to travel concurrently with the beam, so that the flux hitting the wall as a given slice of the beam passes through the system is proportional to the line charge density of that beam slice. The number of photons emitted per bunch particle per meter is specified as input to the code. This is multiplied by an assumed quantum efficiency to give the number of electrons produced per meter per

positron. Since the photons hitting the vacuum chamber wall at the position of the simulated system travel with the beam and were produced upstream (in the ILC wiggler this can be considerably upstream), the photons hitting the wall will be a composite of radiation from locations with different magnetic fields. For simplicity, and in order to change only one variable from simulation to simulation, in our calculations we have neglected the change with z of this flux; therefore we do not change the number of photons striking the wall per bunch passage from simulation to simulation as we vary the dipole magnetic field strength. We assume here that all electrons in the system are made by photoemission or by secondary electron emission produced by the impact of electrons at the wall. Ionization of background gas is assumed to be negligible, as are electrons formed by lost beam particles hitting the wall. The photon reflectivity is not known for the ILC damping ring vacuum chamber. In these runs it was assumed to be 1.0-- i.e., the photon impacts were spread evenly around the circumference of the cross section of the vacuum chamber, excepting the entrance to the antechamber (see below). Since, except for electrons very near to the beam, electrons are tied to field lines and remain very near

to the x values at which they are born, this high reflectivity allows for examining dynamics of electrons at all locations in the chamber.

The secondary electron emission model is described in ref. [5]. It is a heuristic model based on fits to experimental data. The coefficients needed by the model were obtained from bench measurements [5] and extrapolation from data from the CERN Super Proton Synchrotron for a stainless steel surface [8], with the peak of the secondary yield vs. energy for normal incidence chosen to be at E_{max}=195 eV and the peak secondary emission at normal incidence set to 1.4. These assumed values are reasonable for typical surfaces. While quantitative details of the phenomenon discussed in this article may depend on the precise parameter values of the SEY model, the essential physics does not.

Numerous simulations were performed in order to find the PIC mesh resolution and time step necessary for accuracy in these runs. This was done by increasing the numerical resolution in space or time until no further change was seen in the time history of the electron cloud buildup. The values chosen can be found in Table 1.

The number of electrons generated is large, and continually increases both the computational time per time step and the memory needed as the simulation progresses. This numerical challenge was handled by “culling” the electron macroparticle population when a certain number (the culling threshold) of macroparticles was reached. At this point a random selection of half of the macroelectrons was removed from the system and the numerical weight (i.e., the number of real electrons per macroelectron) of each of the

remaining macroelectrons was doubled. In order to retain good statistics for electrons newly formed at the wall, new electrons born after culling were given the original weight of electrons born at the beginning of the simulation. This culling operation was found to create large ripples in the average electron density vs. time if the culling threshold was too low. Culling at 40,000 macroelectrons was found to give a low enough level of such noise that the equilibrium density value could be accurately ascertained, so the runs here were done with that threshold.

The vacuum vessel was assumed to be a perfectly conducting circular chamber with radius a=2.3 cm. An antechamber of full height 1 cm was located at the +x midplane. Any electrons hitting this part of the surface were assumed to be lost and produced no secondaries. Note that the ILC damping ring wiggler chamber would have an antechamber on each side of the chamber, but these runs, because they began as a benchmarking exercise, have only a single antechamber on the +x side.

Figure 1 shows the evolution of the electron density with time for B = 0.8 T (i.e., n=137.8), a "high" field in the range where there are no effects of resonances seen in the equilibrium average density, and 0.07 T, a field at which the resonance occurs (n=12). As can be seen in the figure, there are larger fluctuations in the density in the 0.07 T case. The values of equilibrium average density given later in this report were obtained for each simulation by averaging over the last 0.7 μs of the run, giving a value for the 0.07 T case, for example, as shown by the horizontal line in the figure. This small interval was chosen arbitrarily to give an "instantaneous" value of the equilibrium density. If culling

or real dynamics produced significant fluctuations during this interval, the interval was widened enough so that the value was affected by the fluctuations by no more than a few percent.

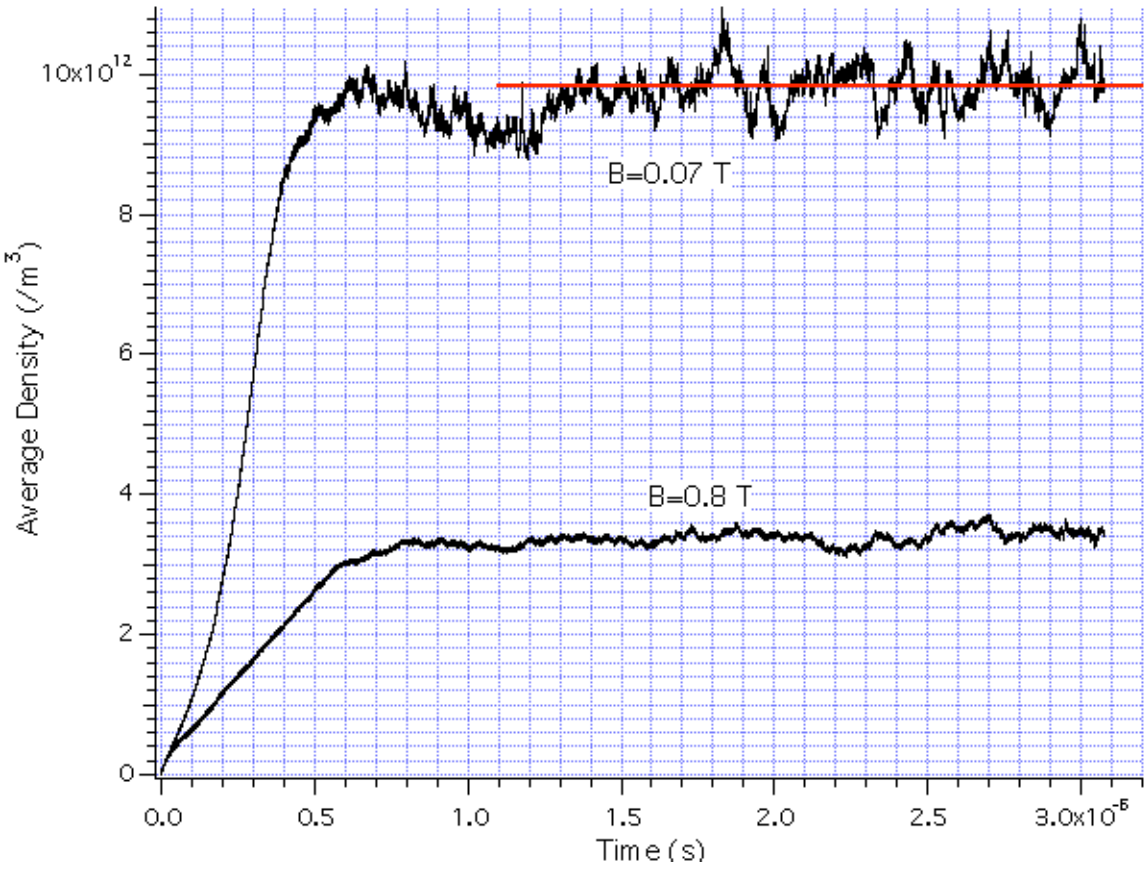

Fig. 1 Build-up of the average density for B=0.07 and B=0.8 T (n=12 and 137.8, respectively). The horizontal line shows the value of the "equilibrium average density" for B=0.07 T.

III. Simulation Results – Electron Cloud Density vs. B

Results of the simulations can be seen in Fig. 2a, where the equilibrium average density for each simulation is graphed vs. the ratio of the bunch spacing to the cyclotron period, which we refer to as "n", following Eq. (1). The “cyclotron period” referred to is the cyclotron period of a non-relativistic electron (γ=1). The abscissa is thus proportional to B. As mentioned above, it is evident from the figure that at the higher fields there is no dependence of the equilibrium average density on B. Below approximately 0.6 T, however, or n < 103, there are very narrow spikes (FWHM ≈ 10 G) where the density rises to approximately three times its value at high B. It is evident from the expanded view in Fig. 2b that these spikes indeed occur where the cyclotron frequency is an integral multiple of the bunch passage frequency. It should be noted that since the spacing between the field values at which such a resonant condition occurs is ΔB=58 G for the bunch frequency used (one bunch passage every 6.15 ns) it was not reasonable to do enough runs to outline all the peaks in the curve. The reader should therefore understand that “+” marks on the curve show the simulations done, and the absence of peaks where there are no markers does not imply that a resonance is missing. Indeed, at every integral multiple of ΔB where we have done a simulation, if B<0.6 T we have found a peak.

Figure 3 is a two-dimensional representation of the spatial distribution of the electrons for the same two cases shown in fig. 1: 0.8 T and 0.07 T. It is time-averaged over the entire time of the simulation. Since most of the 3.2 μs simulation takes place during the plateau of the density, the figure well represents the conditions in that time interval. The

higher-field case exhibits the characteristic “stripes” which are known to occur at the x values where the energy of the electrons striking the chamber wall is near the peak in

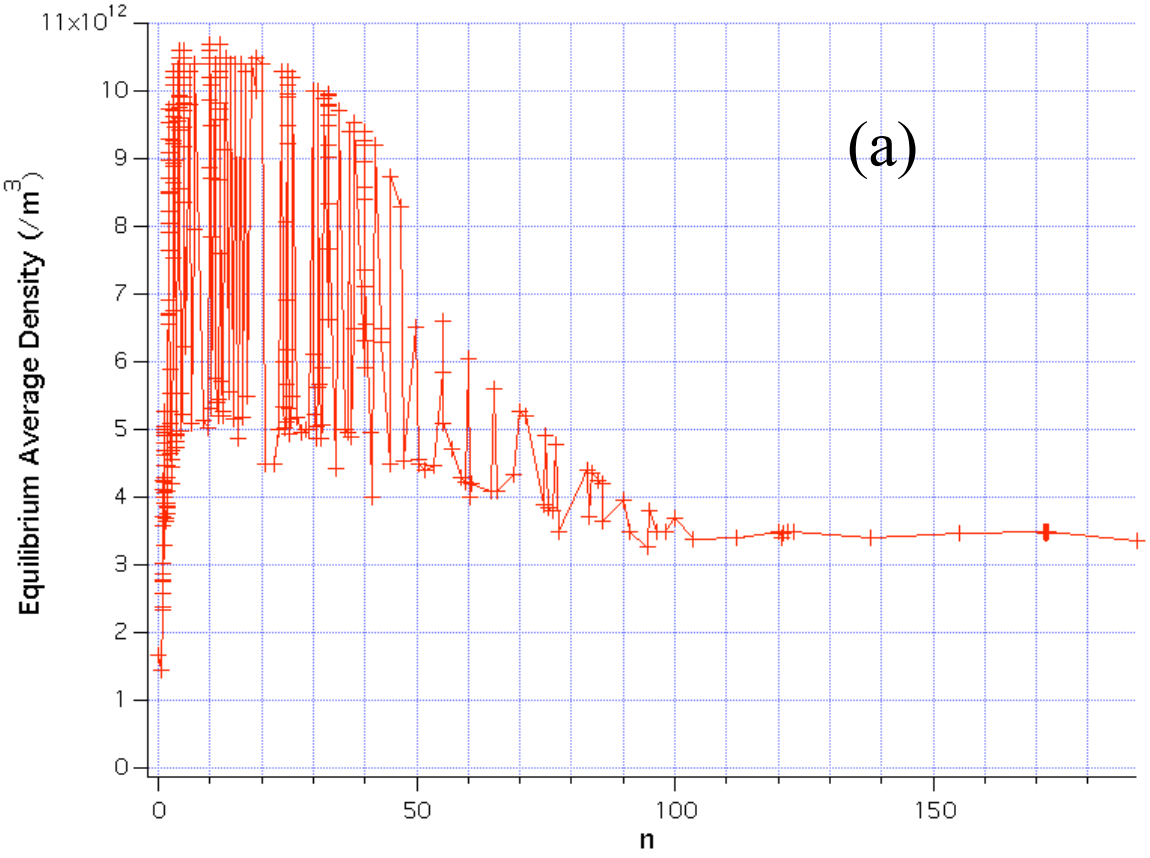

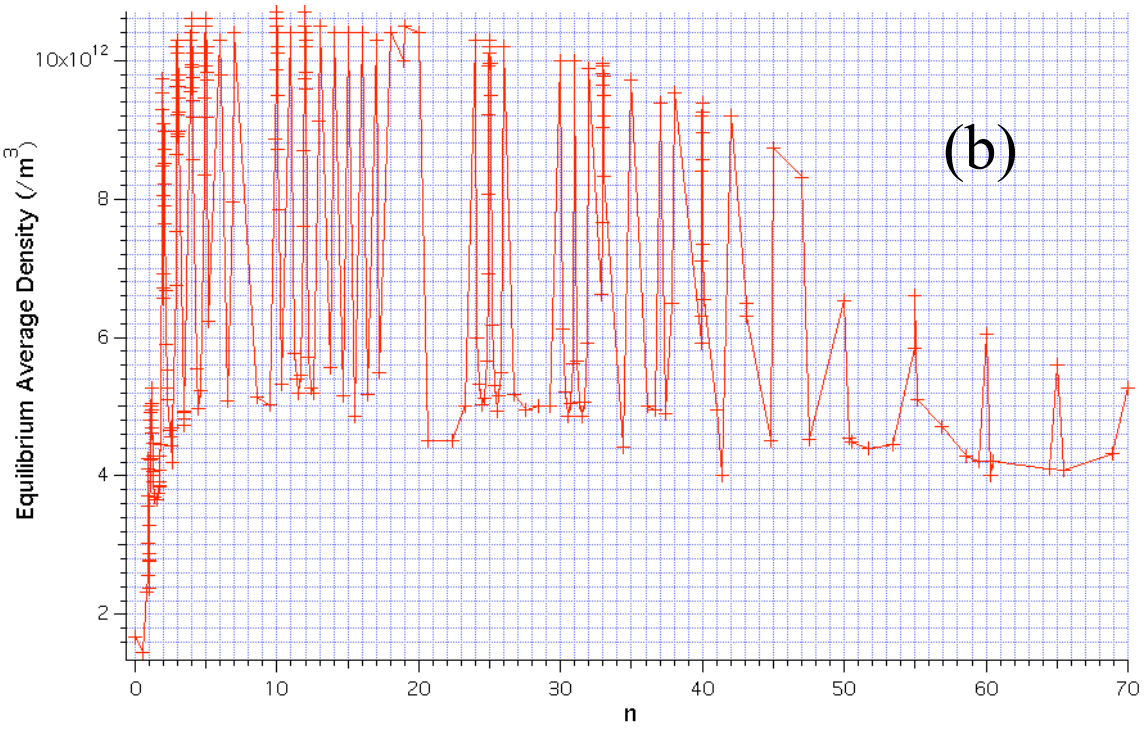
10x10^12
8
6
4
2
Equilibrium Average Density (/m^3)
(b)
0
10
20
30
40
50
60
70
n

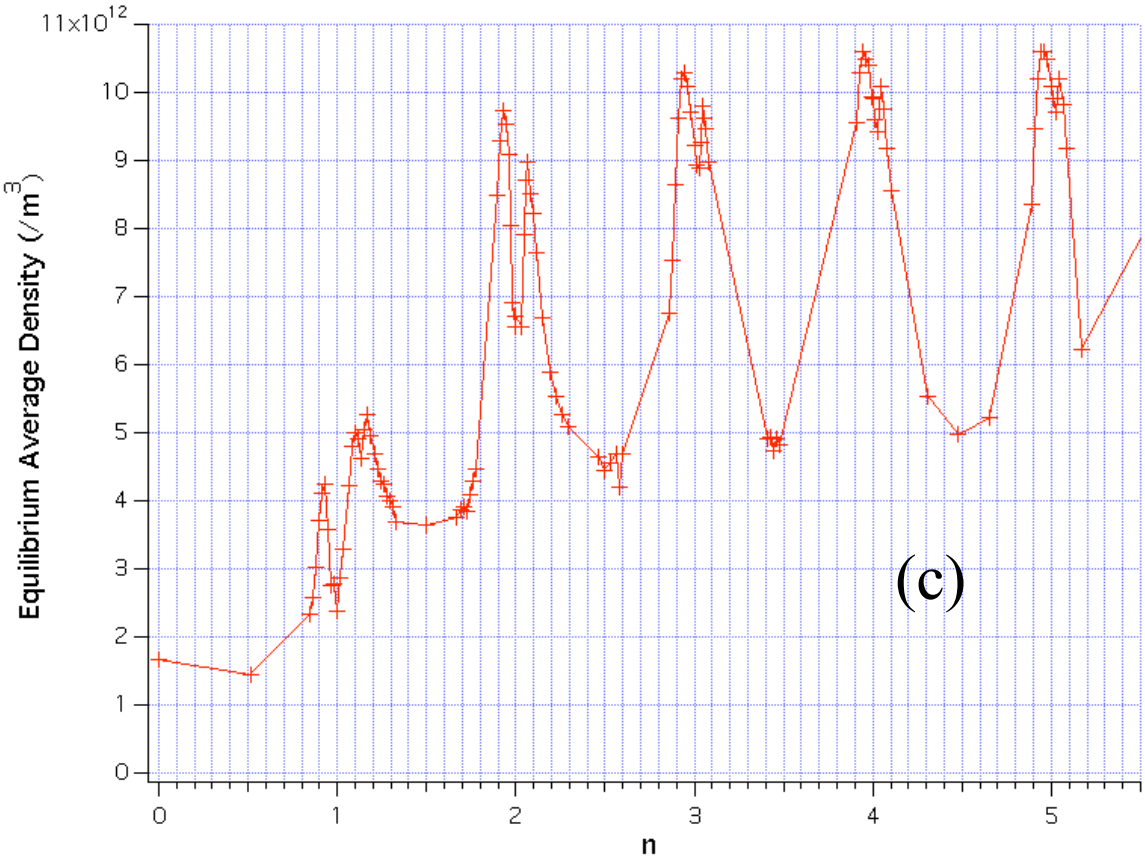
11x10^12
10
9
8
7
6
5
4
3
2
1
0
Equilibrium Average Density (/m^3)
(c)
0
1
2
3
4
5
n

Fig. 2 Equilibrium average density vs. n, the ratio of the bunch spacing to the cyclotron period. Simulations were done only at the plus sign markers, which have been connected by lines to guide the eye. (a) Simulations for $0 \le n \le 189.5$, or $B \le 1.1$ T; (b) $0 \le n \le 70$, showing that peaks in density are at integer values of n; (c) Expansion of the range $0 \le n \le 5.5$ in order to show the minima in the center of these peaks. The depression decreases with increasing n.

the curve of secondary electron yield (SEY) vs. energy [9-11]. (The SEY here is defined as the number of electrons emitted divided by the number of incident electrons.) The resonant case shows electrons that are much more widely distributed. Though the peak local density in the resonant case is lower than for the non-resonant case, their presence over a much larger area results in a larger total number of electrons in the chamber. The fact that the electrons in the resonant case are, on average, farther from the beam than those for the non-resonant case will result in quantitative differences in the effect of the electron cloud on the beam. We have not yet explored effects on the beam; we defer this for future work. Wall heating by electrons is also clearly different in the two cases.

For $n < 12$ there is a density minimum in the middle of the resonant peaks of the equilibrium-density-vs.-B curve, as shown in fig. 2c. This feature disappears as n increases, and is negligible for our parameters for $n > 12$. Possible reasons for this effect and for the disappearance of the peaks at high B will be discussed in Section VI after the dynamics of the electrons for the resonant case have been examined.

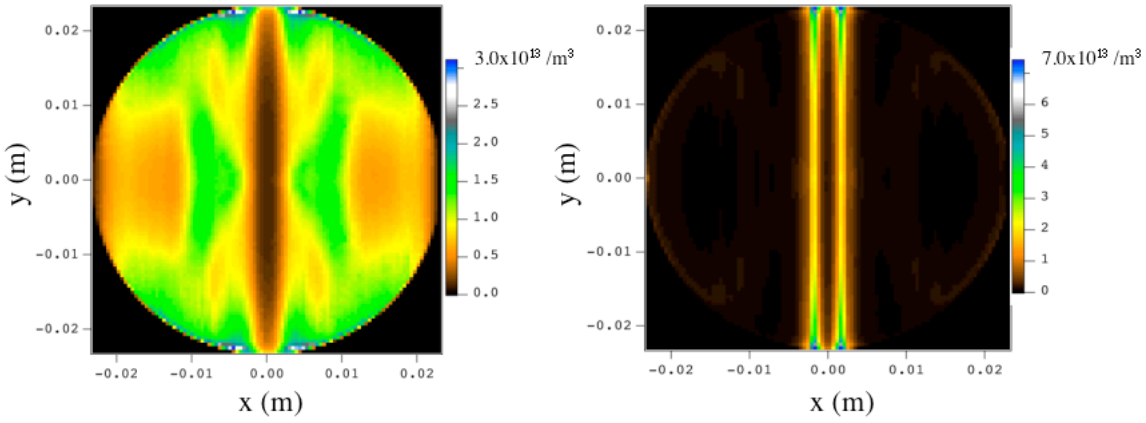

Fig. 3 Density distribution for a resonant (0.07 T) and non-resonant (0.8 T) case. Vacuum chamber is circular and fits exactly within the plot.

IV. Dynamics of the Resonance

In this section we will show the details of the resonance dynamics using the simple case of a system without the electron space charge.

As the beam bunch passes, all of the electrons in the system that are not at the center of the chamber experience a force directed toward the beam. Since the bunch is short and traveling at the speed of light, we will for the moment consider this force to be an instantaneous kick. This approximation will be examined in Section VI. Because the beam is traveling at relativistic speed, the direction of the force is in the x-y plane to a very good approximation. The y component of the force accelerates the electron along

the dipole field lines. The x component affects its cyclotron motion, which is in the x-z plane. As can be seen in fig. 4, the effect of the x kick is to rotate $v_\perp$ toward a direction parallel to the x axis and pointing toward the y axis (i.e., toward the –x direction for an electron with x>0, and +x direction for electron with x<0). If the resonance condition given in Eq. (1) is fulfilled, when the next beam bunch arrives the electron will be at the same position in the x-z plane, and its $v_\perp$ will be rotated again, so that if the electron remains in the system long enough, its $v_\perp$ will end up at 180° to the x axis if the electron is at x>0, and 0° if its x<0. For the beam intensity and chamber size used here, since the electrons are born at the wall with just a few eV of energy, the beam kick is large compared to the initial energy and quickly (in a few bunch passages) should rotate $v_\perp$ into this position. When $v_\perp$ is at 180° to the x axis, the electron is at the bottom (lowest z position) of its cycle, where it has completed 270° of its cyclotron orbit as measured from the x axis. We will call this latter polar angle describing the electron position the "cyclotron phase angle". If the magnetic field is not close to a resonant value, the electron will be at different positions as sequential bunches arrive, with the velocity vector therefore changing its direction between kicks, and the effect of the kicks on the cyclotron motion will therefore tend to average to zero over time.

For the resonant case, each beam kick will increase the magnitude of $v_\perp$ if its x component is in the same direction as the beam force—i.e., if $v_{\perp x} < 0$ for x>0 or $v_{\perp x} > 0$ for x<0. This orientation of $v_\perp$ can occur either due to initial conditions or because the beam kicks have rotated it to this position. The change in $v_\perp$ will also change the

cyclotron radius, as shown in fig. 4. Since the effect of the force of the beam is to rotate the $v_\perp$ into a direction where it will increase in magnitude, the average $v_\perp / v_\parallel$ will increase, and therefore the average cosine of the angle of the electron wall impacts with respect to the normal will decrease, assuming that the electrons stay in the system long enough for the beam to have a significant effect on them. A significant decrease in the average cosine is indeed seen in the POSINST simulations at resonant magnetic fields. The change made in the angle and magnitude of the velocity will result in a change in the position of the gyrocenter (again, see fig. 4). This movement of the gyrocenter is the well-known "ExB guiding center drift".

An individual-particle tracking code was written to elucidate the dynamics described above, which in the real system are complicated by the effect of the spatial dependence of

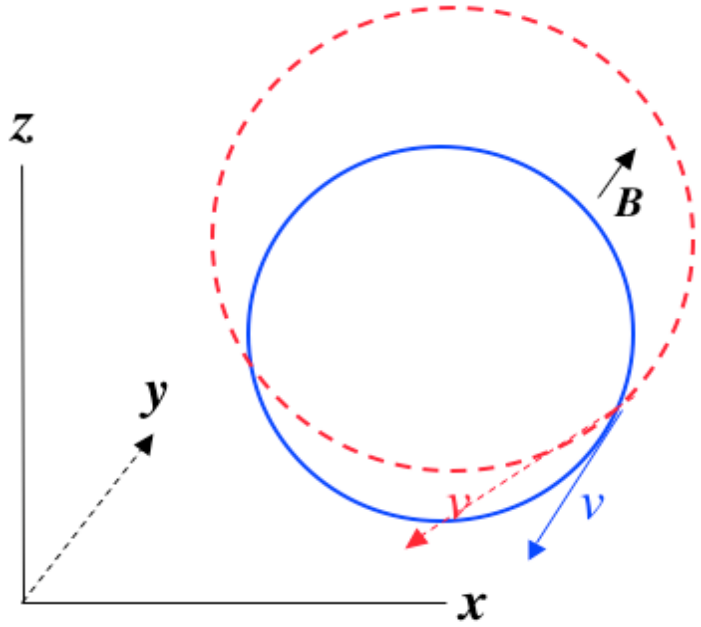

Fig. 4 Electron orbit in the x-z plane (plane perpendicular to B) showing the effect of the beam kick on the cyclotron radius and gyrocenter. The electron has x>0, therefore the beam kick is in the –x direction. Blue is before the kick; red is after. Arrows show rotation of electron velocity by the beam kick.

the kick magnitude on distance from the beam. For simplicity the electron space charge force was neglected (this approximation is good for the initial phase of the cloud buildup), and the beam force was approximated as an instantaneous kick. The Bassetti-Erskine formula [12], integrated over the bunch passage time, was used to calculate the kick. The electrons were tracked in three dimensions, with the vacuum chamber considered to be an infinitely long straight cylinder. Image forces were neglected. All electrons were launched at time=0 from the vacuum wall at the top of the chamber; results for electrons born at the bottom wall are then obvious by symmetry. Likewise, only results for electrons with $x>0$ will be shown, since results for $x<0$ can be deduced by symmetry.

Tracking was first done for a case where the relativistic increase in mass was neglected—i.e., all electrons remained at $\gamma = 1$. While not accurate if electron energies become large, the results illustrate very well the effects described above. And as will be described later, almost all of the electrons remain non-relativistic in the POSINST simulations.

A few percent of the electrons with the right initial conditions were found to oscillate in y for several tenths of a microsecond without striking the wall, due to the restorative nature of the force of the beam. These “survivor electrons” are useful because they display the long-term effects of the beam on the electron dynamics. In fig. 5 the cyclotron phase angle is graphed for these survivors at the time of each bunch passage for the resonant case of n=12 and the non-resonant n=11.5 case. As predicted above, the phase angles (graphed only at the arrival time for each bunch) for the resonant case go to 270°, while they oscillate through the full range from 0° to 360° for n=11.5. The electron energies are found to rise monotonically for n=12, while for n=11.5 energies rise and fall, with the maximum energies much lower than those for the resonant case. It is evident by looking at the energies for the resonant case, however, that for the small percentage that are the "survivors" the energy increases so significantly over the 50-bunch-passages time interval of the single particle calculation that making the nonrelativistic approximation of $\gamma=1$ is inaccurate.

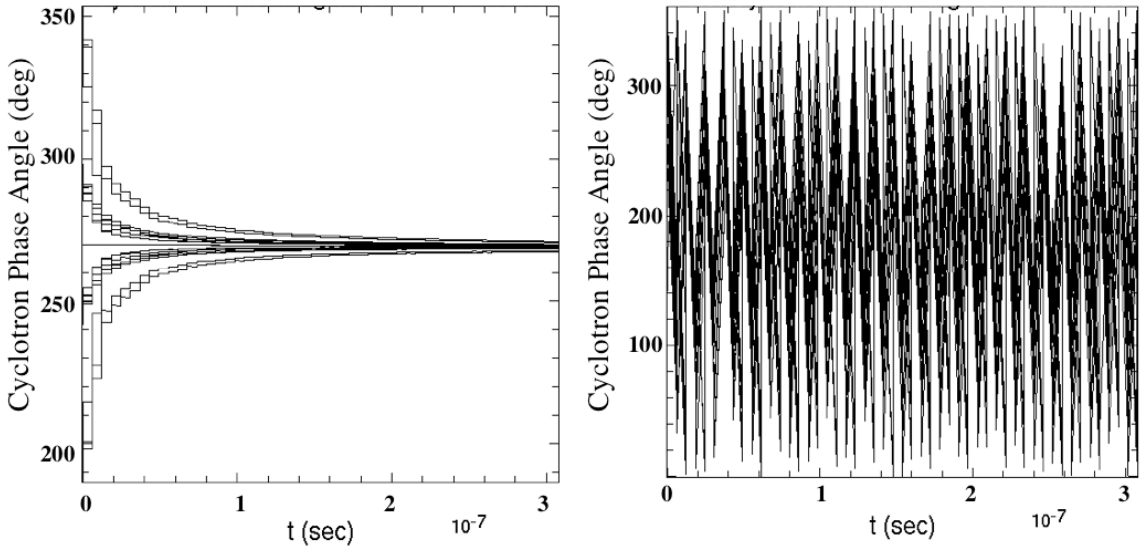

Fig. 5 Change with time of the cyclotron phase angle, plotted at the arrival time for each bunch, for electrons that remain in the system for long times-- resonant and non-resonant case. Dynamics are computed non-relativistically here for simplicity. On the left is n=12.0 (resonant case); on the right is n=11.5.

A fully relativistic tracking calculation shows a somewhat more complicated picture. As the mass of a given electron increases, it detunes from the resonance. Again there is a population of electrons that, as described above, tends to oscillate in y, staying in the system for a few tenths of microseconds before they hit the wall. But in the relativistically correct calculation these have shorter lifetimes (~0.1-0.2 μs, rather than ~0.5 μs, for the n=12 case). Thus these electrons, which stay in the system long enough to acquire a significant energy boost from the beam, hit the wall and produce secondaries much earlier. This would lead to a higher growth rate of cloud density than what would be projected from the nonrelativistic case.

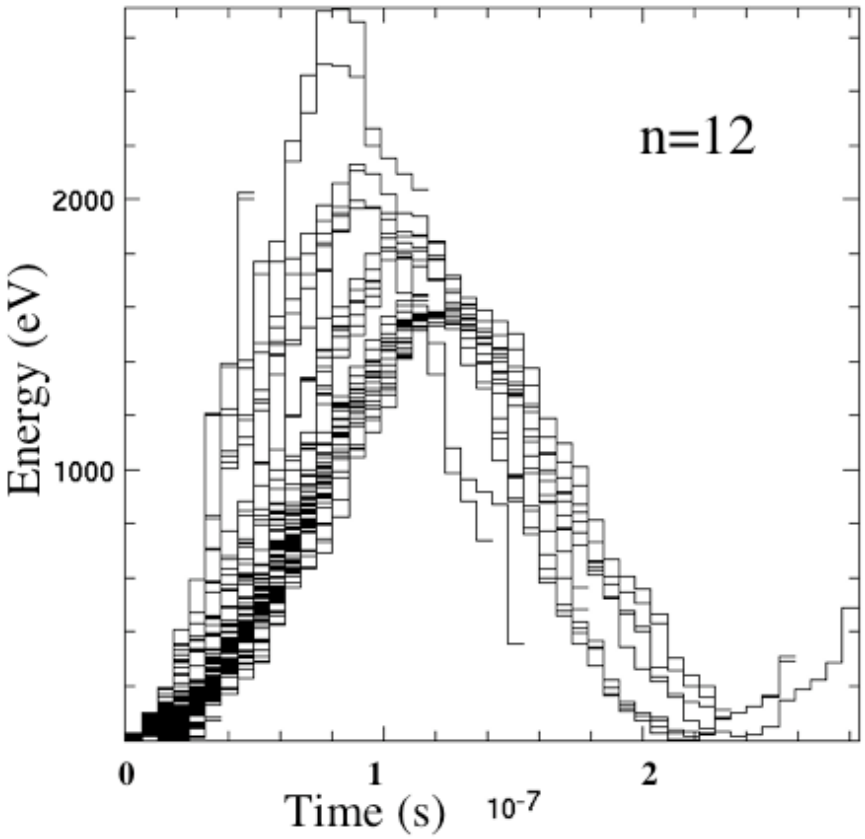

Fig. 6 Kinetic energy of all electrons in the tracking calculation vs. time for n=12, showing oscillation of energy due to detuning from resonance caused by changes in the particle mass. Curves end if the electron hits the wall and leaves the system.

Figure 6 shows the kinetic energy of all of the particles. Clearly visible is the long-term detuning from the resonance, which causes a slow oscillation in the energy. Histograms of the final energies for a resonant and non-resonant case (n=12 and n=11.5) are shown in fig. 7 for electrons that hit the wall during the 0.3 μs covered by the calculation. The two cases have different distributions of energies, but the average energy is almost the same (95 eV for the n=12 case and 94 eV for n=11.5). This also occurs in the POSINST simulations of these cases. In the resonance case there are more electrons for almost any

energy above 50 eV, especially in the range of 50-125 eV. Given the dependence of the SEY on energy, and the fact that the higher $v_\perp$ acquired at resonance implies a shallower impact angle at the wall, this spectrum indicates that the n=12 case will produce more electrons.

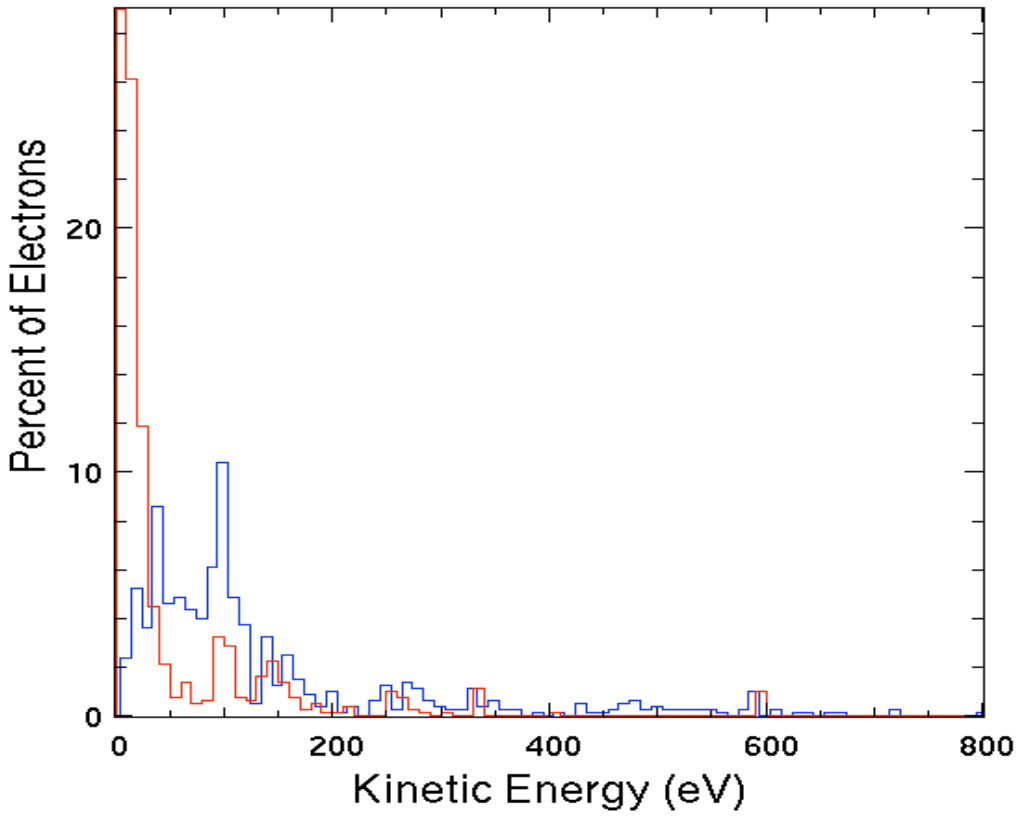

Fig. 7 Histogram of final kinetic energies for a resonant (n=12.0, blue) and non-resonant (n=11.5, red) case for electrons that hit the wall during the 0.3 microseconds simulated. Calculated with single particle tracking code with correct relativistic dynamics. Histogram bins are 10 eV wide.

Figure 8 shows the evolution of the cyclotron phase angles (plotted only at the bunch arrival times) with time in the relativistically correct calculation. Again the detuning

from resonance with relativistic mass increase is evident. Phase angles for the electrons go to 270°, but then move slowly away from this value as the mass increases. Note that

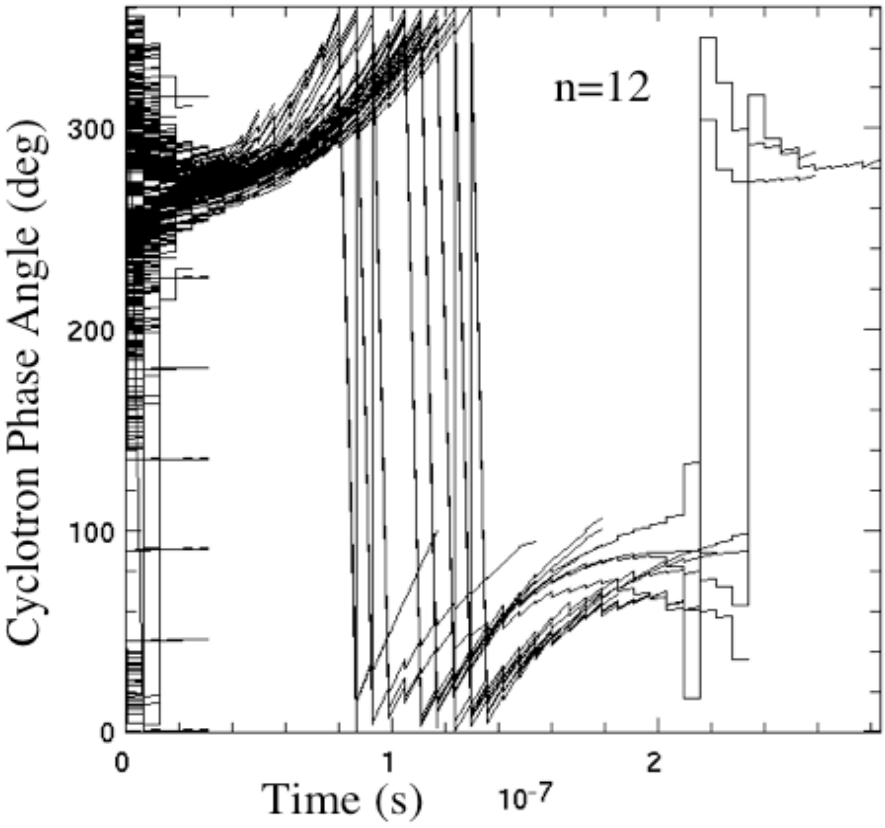

Fig. 8 Cyclotron phase angle for each electron at the time of a bunch arrival vs. time for n=12. Phase angles are pushed by the resonance to 270 degrees, and then move away from this value as the electron mass increase detunes it from resonance. Curves stop when the electron hits the wall and leaves the system.

since the phase angle is modulo 2π there are a few instances, especially near t=2 μs, where the value shown seems to decrease suddenly by an integral multiple of 360 degrees.

Though the dynamics in these simple tracking calculations have been simplified by the use of the beam kick approximation and neglecting the electron space charge force, the results clearly show and elucidate the dynamics of a resonance where the beam bunch frequency equals an integral multiple of the cyclotron frequency. The energy distribution of the electrons is changed at resonance to one which raises the effective SEY. Since $v_\perp$ is increased, the electrons will also, on the average, hit the wall at shallower angles, which also increases the effective SEY.

V. Comparison of Simulation Results to Single Particle Tracking

The complete POSINST simulations include the space charge force from the electrons and the effect of a finite-length beam, both of which are not present in the single particle results of the last section. Therefore in this section we use the results of the last section to identify quantities of interest in the POSINST simulations and examine the agreement between the results of the full simulations and the simple single-particle model.

Figure 9 shows the energy spectrum for n=11.5 and n=12 from POSINST simulations for electrons striking the vacuum wall during time interval 0-0.2 μs, i.e., during the cloud buildup. The spectrum is quite similar to that shown in Fig. 7. From the resonance concept and also the single particle tracking results we expect this to be due to an increase in perpendicular momentum for the resonance case. Indeed, inspection of the

spectra of v_y for various x for these electrons shows very little difference between the resonance and non-resonance cases. But as shown in Fig. 10, the perpendicular velocity is enhanced in the resonance case, and the cosine of the angle of impact is less, which also increases the effective SEY.

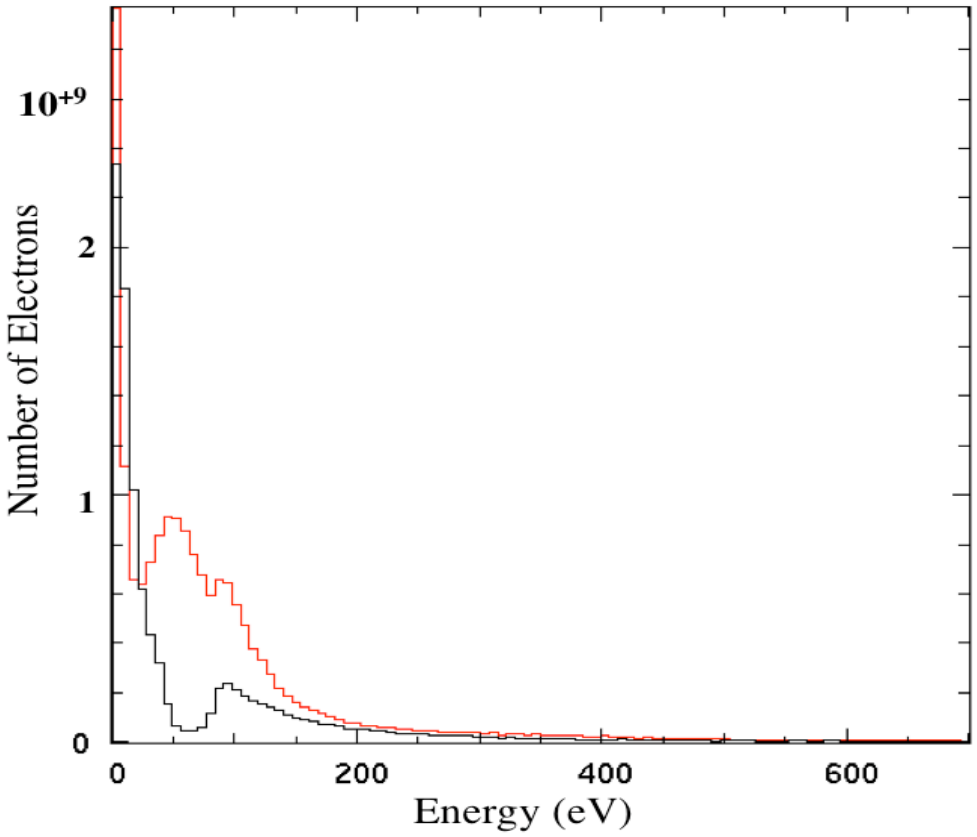

Fig. 9 Energy spectrum from POSINST simulations of electrons hitting the wall for the time interval from 0 to 0.2 μs for n=11.5 (black) and n=12 (red).

Figure 11 shows the perpendicular velocity distribution in various x ranges for n=11.5 and n=12. Note that for the resonance case the spatial distribution of electrons with large

$v_\perp$ is quite wide in x, which is consistent with the density distribution of Fig. 3. Knowing the workings of the resonance mechanism, this distribution can now be explained. We can approximate the x component of the force of the beam on the electrons, F_x, as that of

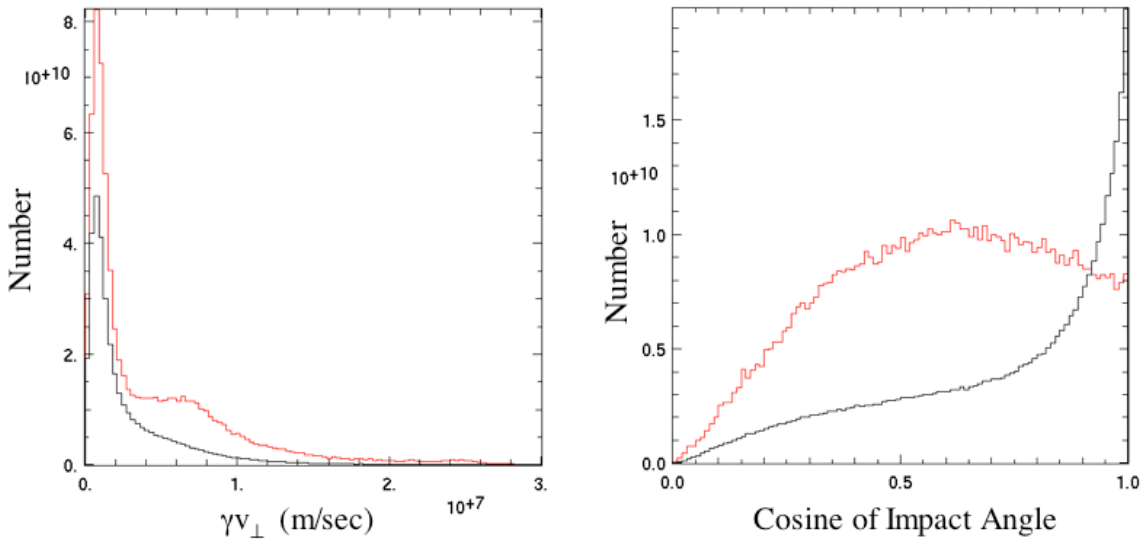

Fig 10. Histograms for n=11.5 (black) and n=12 (red) for electrons hitting the wall in POSINST simulations in the time interval from 2 to 3 μs (which is after the cloud density has reached equilibrium). Shown are the number of electrons hitting the wall vs. $\gamma v_\perp$ (left) and the cosine of the impact angle with the wall with respect to the normal (right).

an infinite line of charge at x=y=0, which is an excellent approximation for most of the vacuum chamber, where $r>>\sigma_x$ and $r>>\sigma_y$. Then the contours of constant F_x are circles tangent to the y axis. For an x velocity change for a given beam kick integrated over one beam passage equal to Δv_x these circles have radius

$$r_{Fx} = \frac{e\lambda_0\sigma_z}{\sqrt{8\pi}\,\varepsilon_0 m_e c \Delta v_x} ,$$

where λ_0 is the line charge density at the center of the bunch and ε_0 is the permittivity of free space. The centers of the circles are located at $(x,y)=(\pm r_{Fx}, 0)$. The kick in y is similar, with the contours being circles with radii given by the same formula (Δv_y replacing Δv_x). But in this case the circles are tangent to the x axis, with centers at $(x,y)=(0, \pm r_{Fy})$. Thus the area of the contours of a given Δv_x extends twice the distance in x as the contours for the same Δv in the y direction. Because at field values where there is a resonance the x component of the force of the beam as well as the y component increase the energy of the electron, whereas in the non-resonance case only the y force component is effective, the distribution of electrons with enough energy to effectively produce secondaries therefore is wider in x in the resonance case. This is also reflected in Fig. 12, which shows color contour plots of electron energy, averaged over the time period of the simulation, for n=11.5 and n=12. Note the horizontal bi-lobe pattern for the resonance case, whereas for the off-resonance case the contour areas are vertically aligned except very near the beam.

For $x \leq 2$ mm Fig. 11 shows no growth in $v_\perp$ for the resonance above what is seen in the non-resonant case. We attribute that to the fact that, as seen in Fig. 3, for the resonance case there are few electrons in this region except at high y, where the x component of the beam force is small.

Both the single particle tracking calculations and POSINST simulations show that almost all electrons remain in the simulations for less than 7 bunch passages and never reach high v/c.

We conclude that the dynamical features shown by the single particle tracking are represented in the full simulations, giving further credence to the resonance explanation and to the details of the electron dynamics shown in Section IV.

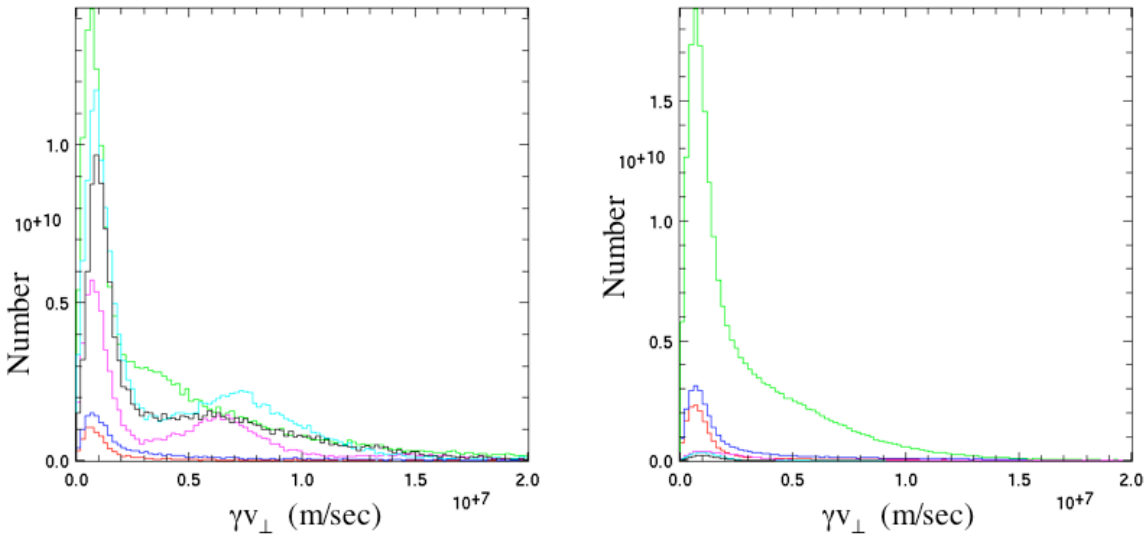

Fig. 11 Histograms from POSINST simulations showing the number of electrons which hit the wall in the time interval between 1.2 and 3 μs with a given $\gamma v_\perp$ for n=12 (left) and n=11.5 (right). Each curve shows the $v_\perp$ distribution function for a different range of x: 0≤x≤1 mm (red), 1≤x≤2 mm (blue), 2≤x≤7 mm (green), 7≤x≤10 mm (magenta), 10≤x≤15 mm (cyan), 15≤x≤20 mm (black).

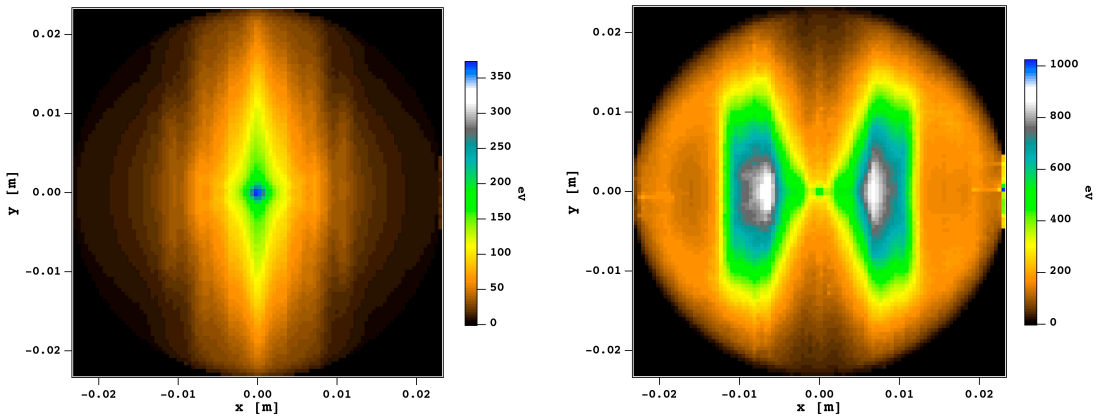

Fig. 12 Color contour plots of the average energy of electrons, averaged over the time period of the simulation (0-3 μs) shown as a function of x and y for n=11.5 (left) and n=12.0 (right) from POSINST simulations.

VI. Discussion of Features at High and Low B

It remains to explain special features of the equilibrium density vs. B dependence, such as why no such effects are seen at the higher magnetic fields, e.g., above 0.6 T in fig. 2, and why there are "double" peaks, with a local minimum near the resonance, for low B. In this section we attempt to understand these aspects of the problem.

We first discuss the absence of peaks at high magnetic field. We have assumed in the discussions above that the force of the beam on the electrons is an instantaneous kick. Given this assumption, at resonance each time a bunch appears the electron is at the same

position, and the dynamics are as we have described, until the relativistic mass increase gradually detunes the electron from resonance. The assumption of an instantaneous beam kick is good when the time for the bunch to pass an electron is much less than the smallest relevant timescale in the problem, the cyclotron period. Thus the assumption is good when

$$B << 2\pi \frac{m_e c}{e l_b} \qquad (2)$$

where l_b is the bunch length and c is the speed of light. As B increases, the cyclotron period decreases until equation (2) is no longer valid. Instead the beam force during one bunch passage is integrated over a significant fraction of the cyclotron rotation. The concept of a "resonance" becomes invalid. The effect of the beam force is added to a velocity whose direction is changing with time, and it will therefore add less to the magnitude of the velocity. For high enough B the net effect will be negligible. For $l_b \sim 4$ σ_z the condition of Eq. (2) fails in the same range where the amplitude of the peaks in fig. 2 decreases to zero. To our knowledge the resonance we discuss here has not been discussed in the literature of the electron cloud before. That is presumably because in the parameter regimes of the accelerators that have been studied the bunch length was longer, and the magnetic fields studied were perhaps higher, so that Eq. (2) did not hold.

The energies of electrons in the simulations were for the most part less than about 600 eV, so that the electrons are essentially nonrelativistic. For large enough B, however, the small change in γ, and therefore in the cyclotron frequency, can still lead to a nonnegligible detuning from resonance, because there will be many cyclotron orbits

between bunch passages. This will be another contributing factor to the decrease in peak amplitude at high B. However most electrons exit the system in 3-4 bunch passages. Thus the effect will only be significant for electrons of several hundreds of eV.

We turn now to the question of why the low-n peaks in the density vs. B curve have a minimum at resonance. To investigate this we have extensively compared POSINST simulation data for n=2 with results at the nearby off-resonance peak (n=1.93). The data show that at resonance the electrons do attain higher $v_\perp$ than in the off-resonance case, but this happens because they remain in the system longer, building up energy with each bunch passage. As a result, while their average SEY is slightly higher than for the electrons in the off-resonance case (1% higher during the cloud buildup phase), they hit the wall a lot less often (rate of wall bombardment is 23% lower than for the non-resonance case), therefore producing fewer secondaries. As n increases, this difference in the bombardment rate decreases. For n=5 and the off-resonance peak at n=4.96, for instance, where the minimum at resonance is a lot shallower than at the n=2 resonance, the difference in bombardment rate is only 0.5%. Thus the longevity of the electrons at resonance at low n accounts for the minimum in cloud density there.

Before the simulation data mentioned above were analyzed, one possible explanation for the low-n minima at resonance seemed to be that the action of the resonance might cause electron energy to increase past E_{max}, resulting in electrons with a smaller effective SEY than for the case just off resonance. This did not prove to be the case—the SEY for the high-$v_\perp$ electrons at resonance was still near the peak, partly because their impact angle

was lowered by the increase in perpendicular energy (see Fig. 13 for SEY vs. energy and impact angle).

The divergence between the cloud density vs. time curves for n=2 and n=1.93 occurs after space charge forces becomes important. Therefore a detailed quantitative explanation of the variation of the longevity difference with n, including its behavior in the vicinity of a resonance, would be likely to require solution of the full dynamics of the electron motion in the presence of spatially nonuniform and time-varying space charge. We have not attempted to solve this problem in this report, and leave it for future work.

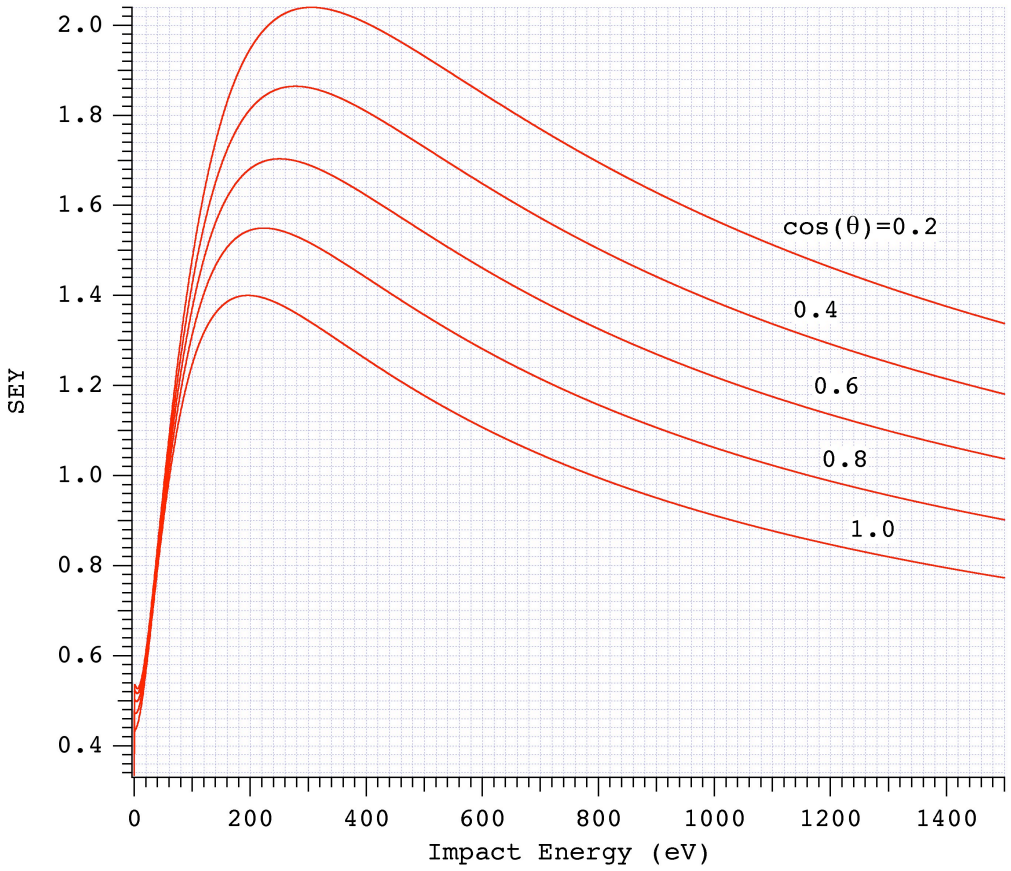

Fig. 13 SEY vs. Impact Energy for our parameters

In considering the peaks at low B it should also be mentioned that at lower order resonances (i.e., low n) the dynamics can be influenced by finite gyroradius effects. Electrons with perpendicular energy of 300 eV seen in simulations at n=12 have gyroradii of 0.84 mm. At n=1, the gyroradius of such an electron would be 1 cm, which is 43% of the chamber radius. This effect could cause early loss of electrons with similar and higher energies. We believe that this large-gyroradius effect causes the decrease in the peak amplitude seen when going from n=4 to n=1. Comparing simulations at n=1 and n=2 we see many more electrons with energies above 100 eV (gyroradius at n=1 of 0.58 cm, and 0.29 cm for n=2) in the n=2 case, and the average energy of electrons hitting the wall is 118 eV for n=1 and 180 eV for n=2. Electrons with the same $v_\perp$ for the two cases also on average remain in the simulation longer in the n=2 case. Finally, simulation energy spectra show many more high-energy electrons hitting the wall for n=2 than for n=12, though there are more higher energy electrons confined in the chamber in the n=12 case.

VII. Single-particle analysis.

Certain features of our results, such as the suppression of the effect for long bunches, the energy gain of the electrons at resonance, and the phase alignment, can be readily derived from the single-particle dynamics. In order to simplify the calculations, we linearize the single-electron equations of motion by making the following assumptions: (1) the

electrons remain nonrelativistic even at resonance; (2) space-charge forces, as well as image-charge forces from the vacuum chamber, can be neglected; (3) the cyclotron gyroradius is small compared to the chamber radius; (4) $\sigma_t << \tau_b$, where σ_t is the RMS bunch duration; (5) we do not include electron motion which impacts the chamber walls, and (6) we restrict our attention to only those electrons with small vertical amplitude. Although these approximations restrict parameter values (e.g., B cannot be too small), and the electron's phase space and time histories, they allow for a qualitative explanation of the resonance behavior at small B and its suppression at high B (or for long bunches). The line charge density of the positron beam at time t and longitudinal location z is given by

$$\lambda(z,t) = eN_b \sum_{k=0}^{\infty} \frac{e^{-(z-ct+kc\tau_b)^2/(2\sigma_z^2)}}{\sqrt{2\pi}\sigma_z} \tag{3}$$

where the summation is over successive bunches. We choose the origin of time such that the center of the first bunch (k=0) crosses z=0 at t=0. At this instant, the centers of bunches k=0,1,2,3,... are located at $z = -kc\tau_b$. While in a real accelerator the number of bunches is finite, the infinite upper limit in the above summation does not affect the results in the analysis that follows.

The electric field generated by the beam is

$$\mathbf{E}(x,y,z,t) = \frac{\lambda(z,t)}{4\pi\varepsilon_0}\mathbf{G}(x,y) \tag{4}$$

where $\mathbf{G}(x,y)$, with dimensions of 1/length, is the 2-dimensional Bassetti-Erskine field. Under our stated assumptions, the equations of motion for a single electron (charge $-e$ and rest mass m_e) are

$$\dot{\mathbf{p}} = -e(\mathbf{E} + \mathbf{v} \times \mathbf{B}) \tag{5}$$

where $\mathbf{p} \cong m_e\mathbf{v}$ is its momentum. The magnetic field $\mathbf{B}$ has an external component $\mathbf{B}=B\,\hat{y}$ plus the contribution generated by the beam, $\mathbf{B_b} \approx -\hat{z} \times \mathbf{E}/c$. The contribution from this latter component to the $\mathbf{v}\times\mathbf{B}$ force is at most $e\beta E$ (where $\beta=v/c$), hence down by a factor of v/c relative to the electric force, hence negligible in magnitude compared to $\mathbf{E}$. Very near to the beam, especially for low values of the dipole field, the magnetic field of the beam will change the direction of the B field for the short time that a bunch is present. This effect is not present in the POSINST calculations or in this analysis, and will be explored in future work.

Eq. (5) then becomes

$$\begin{aligned} \dot{v}_x &= -(e/m_e)(E_x - v_z B) \\ \dot{v}_y &= -(e/m_e)E_y \\ \dot{v}_z &- (e/m_e)v_x B \end{aligned} \tag{6}$$

We first neglect the field from the beam. The equations become

$$\begin{aligned} \dot{v}_x &= \omega v_z \\ \dot{v}_y &= 0 \\ \dot{v}_z &= -\omega v_x \end{aligned} \tag{7}$$

where $\omega=eB/m_e$. The solution in the x-z plane is

$$\begin{aligned} v_{f,z} &= -\omega\rho_0 \sin(\omega t + \phi_0) \\ v_{f,x} &= +\omega\rho_0 \cos(\omega t + \phi_0) \end{aligned} \tag{8}$$

where the subscript "f" stands for "free" (i.e., in the absence of the beam). The gyroradius ρ_0 is determined by the initial condition, $\omega\rho_0 = v_{\perp 0}$, where $v_{\perp 0}$ is the initial speed in the *x*-*z* plane; ϕ_0 is the initial phase. The solutions for x and z are:

$$\begin{aligned} z_f(t) &= z_c + \rho_0 \cos(\omega t + \phi_0) \\ x_f(t) &= x_c + \rho_0 \sin(\omega t + \phi_0) \end{aligned} \tag{9}$$

where $(z_c, x_c) = (z_{f,0} - v_{f,x0}/\omega,\ x_{f,z0} + v_{f,z0}/\omega)$ is the gyrocenter in the (x-z) plane expressed in terms of the components of the velocity at t=0. As for the motion in y, it is free-particle motion: $v_y = v_{y0}$ and $y = y_0 + v_{y0}t$.

Now taking *d/dt* of the 3rd component of Eq. (6) and combining it with the 1st yields

$$\ddot{v}_z + \omega^2 v_z = \frac{\omega^2 E_x}{B} = \frac{eN_b\omega^2 G_x(x,y)}{4\pi\varepsilon_0 B} \sum_{k=0}^{\infty} \frac{e^{-(z-ct+kc\tau_b)^2/(2\sigma_z^2)}}{\sqrt{2\pi}\,\sigma_z} \tag{10}$$

Under our stated assumptions we can derive an approximation to this equation by setting *x*, *y* and *z* in the right-hand side to their values at t=0, keeping only the essential time dependence in the exponential factor. Without any loss of generality we choose z_0=0, hence

$$\ddot{v}_z + \omega^2 v_z \approx \frac{eN_b\omega^2 G_x(x_0,y_0)}{4\pi\varepsilon_0 Bc} \sum_{k=0}^{\infty} \frac{e^{-(t-k\tau_b)^2/(2\sigma_t^2)}}{\sqrt{2\pi}\,\sigma_t} \tag{11}$$

which is the equation for a driven harmonic oscillator. We readily find $v_z = v_{f,z}(t) + v_{d,z}(t)$, where the free part, v_f, is given by Eq. (8) and the driven part is given by

$$v_{d,z}(t) = \theta(t)\kappa N_b r_e c\, G_x(x_0,y_0)\, A(K,n) \sin(\omega t - \pi n K) \tag{12}$$

where $\theta(t)$ is the conventional step function, $\kappa = e^{-(\omega\sigma_t)^2/2}$, K is the largest integer $\le t/\tau_b$, $n = \omega\tau_b/2\pi$, $r_e = e^2/(4\pi\varepsilon_0 m_e c^2) \approx 2.82\times10^{-15}$ m is the classical radius of the electron, and the amplitude A is given by

$$A(K,n) = \frac{\sin(\pi n(K+1))}{\sin(\pi n)}. \tag{13}$$

To complete the derivation we note that the 3rd component of Eq. (6) is $m_e \dot{v}_z = -eB\dot{x}$, hence $x(t) = x_0 - (v_z(t)-v_{z0})/\omega$. We obtain $v_x(t) = v_{f,x}(t)+v_{d,x}(t)$, where

$$v_{d,x}(t) = \theta(t)\kappa N_b r_e c\, G_x(x_0,y_0)\, A(K,n)\cos(\omega t - \pi n K) \tag{14}$$

and $z(t) = z_f(t)+z_d(t)$ and $x(t) = x_f(t)+x_d(t)$ where the driven parts are given by

$$\begin{aligned} z_d(t) &= -\theta(t)\kappa N_b r_e c\, G_x(x_0,y_0)\, A(K,n)\cos(\omega t - \pi n K)/\omega \\ x_d(t) &= +\theta(t)\kappa N_b r_e c\, G_x(x_0,y_0)\, A(K,n)\sin(\omega t - \pi n K)/\omega \end{aligned} \tag{15}$$

The 1st-order equation for motion in y can be obtained in similar fashion, but it does not add much useful information to the discussion. One finds that those electrons for which the x component of the gyrocenter, x_c, is comparable to or slightly smaller than the chamber radius a oscillate harmonically about y=0 with an angular frequency

$$\omega_y \approx \sqrt{\frac{2N_b r_e c}{x_c^2 \tau_b}} \tag{16}$$

but those electrons whose gyrocenter x_c is within ~a/2 of the pipe center (x=0) are very unstable under the action of the beam, and are driven to the wall of the chamber within one to a few bunch passages (for the parameter values in Table 1).

Equations (12), (14) and (15) are the basic result of this analysis. The amplitude *A(K,n)* is responsible for the linear growth in time of the motion whenever $n = \omega\tau_b/2\pi$ is an integer, because in this case $|A(K,n)|$=K+1, which grows with time. Thus the driven component of the amplitude quickly dominates the motion, the initial phase ϕ_0 and amplitude $\omega\rho_0$ become irrelevant, and the phase of the horizontal velocity (Eqs. (12) and

(14)) is uniquely determined by the beam driving force. One readily finds from Eqs. (12-14) that the phase advance relative to the x axis, from the time a bunch passes until v_z becomes aligned with the beam motion is $\omega\Delta t = (3/4)\times 2\pi$ for $x_c>0$ and $\omega\Delta t = (1/4)\times 2\pi$ for $x_c<0$, in agreement with the single-particle tracking analysis presented in Sec. IV, where Δt is the corresponding time interval. To reach the above conclusion, one needs to recall that the Bassetti-Erskine field component $\mathbf{G}_x$ has the same sign as x. For integer n, the electron energy therefore grows like $|A|^2 \sim t^2$, explaining why in this case the electron-wall collision energy is larger than for non-integer n. Finally, if the bunch length is too large, or the B field too strong, the resonant growth of the amplitude is suppressed by the phase-averaging factor $\kappa = e^{-(\omega\sigma_t)^2/2}$ [11].

VIII. Conclusions

We have described a resonance when the beam bunch frequency is an integral multiple of the cyclotron frequency that causes an enhancement of the electron cloud density. Single particle tracking shows the effect clearly, and though the dynamics are more complicated when electron space charge is taken into account, POSINST simulations, which include space charge, show an increased cloud density at magnetic field values where the resonance condition holds, and perpendicular velocity and impact angle increase consistent with the resonance. One would expect to see the effects of this resonance in real systems in low-field dipoles, in the fringe fields of dipoles, and in the low-field areas

of wigglers for accelerators, storage rings, and damping rings with positively-charged beams and short bunch length. The resonance has not been described previously in the electron cloud literature, probably because it occurs only for relatively low magnetic field values and bunch lengths sufficiently short that the time it takes for the beam to pass an electron is short compared to the cyclotron period.

The resonance has a very big effect on the spatial distribution of electrons in the vacuum chamber. At resonance the electrons are much more distributed throughout the chamber, not confined to the narrow stripes seen in the off-resonance case. This should be taken into account when locating electron cloud diagnostics, which are often placed with the characteristic stripes pattern in mind. Placing the diagnostics in the narrow x range appropriate for the off-resonance case will lead to a large underestimate of the cloud density and misunderstanding of its distribution and therefore its effect on the beam. Different ranges of $v_\perp$ also tend to be found in different ranges of x for the resonant case, which implies a different distribution of wall heating due to the electron cloud.

The importance of the resonance, and the resultant density enhancement, is hard to gauge without the results of complete three-dimensional simulations. In 3D the ExB drift would push electrons in z, so that they would move in and out of resonance. This would probably decrease the density enhancement, but could possibly increase it by bringing more electrons into resonance. It should be noted that because the resonances can be quite narrow in B, 3D simulations of this effect must have enough z resolution to resolve well the gradient in the magnetic field in z. In a more realistic simulation there will also

be some variation of B across the chamber, which will decrease the number of electrons in resonance. If the resonance effect is not decreased significantly in 3D, it could be an important factor in beam dynamics in cases where it produces an electron density that changes with a regular periodicity in z. In the wiggler case, for instance, the electron density would have the same periodicity as the wiggle of the beam centroid, and could cause a resonant deflection of the centroid. The effect of the resonance on cloud buildup was studied here. Its effect on the beam will be deferred for future work.

References

[1] The topic has been the subject of a series of dedicated workshops, the most recent one being ECLOUD07, Proc. International Workshop on Electron-Cloud Effects ``ECLOUD07" (Daegu, S. Korea, April 9-12, 2007). KEK Proceedings 2007-10, December 2007; H. Fukuma, E. S. Kim and K. Ohmi, eds. http://chep.knu.ac.kr/ecloud07/

[2] W.M. Sharp et. al., Proc. of the 2007 Particle Accelerator Conf., Albuquerque, NM, USA, http://accelconf.web.cern.ch/AccelConf/p07/PAPERS/THPAS050.PDF

[3] M. A. Furman and G. R. Lambertson, ``The Electron Cloud Effect in the arcs of the PEP-II Positron Ring," Proc. Intl. Workshop on Multibunch Instabilities in Future Electron and Positron Accelerators ``MBI-97" (KEK, Tsukuba, Japan, 15-18 July 1997; Y. H. Chin, ed.), KEK Proceedings 97-17, December 1997. http://www-acc.kek.jp/WWW-ACC-exp/Conferences/MBI97-N/MBI97.html

[4] M. A. Furman, ``The electron-cloud effect in the arcs of the LHC," LBNL-41482/CBP Note 247/CERN LHC Project Report No. 180, May 20, 1998.

[5] M.A. Furman and M.T.F. Pivi, PRST-AB **5**, 124404 (2002).

[6] G. Rumolo and F. Zimmerman, "Interplay of Ionization and Sputtering with the Electron Cloud", CERN-SL-2001-014-AP.

[7] Y.Cai, M. Pivi, and M.A. Furman, PRST-AB **7**, 024402 (2004).

[8] J. M. Jimenez et. al., ``Electron cloud with LHC-type beams in the SPS: a review of three years of measurements," LHC Project Report 632, 8 April 2003.

[9] F. Zimmermann, ``A Simulation Study of Electron-Cloud Instability and Beam-Induced Multipacting in the LHC," SLAC-PUB-7425, LHC Project Report 95, 27 February 1997.

[10] M. A. Furman and G. R. Lambertson, ``The Electron-Cloud Instability in PEP-II," LBNL-38220/PEP-II AP 96-03/CBP Note-173, June 1996. Proc. EPAC96.

[11] M. A. Furman and G. R. Lambertson, ``The Electron-Cloud Instability in PEP-II: an Update," LBNL-40256/CBP Note-224/PEP-II AP note 97.07, Proc. PAC97

[12] M. Bassetti and G. A. Erskine, \Closed Expression for the Electric Field of a Two-Dimensional Gaussian Charge," CERN-ISR-TH/80-06.